Journal of Hydrology 659 (2025) 133282

Contents lists available at ScienceDirect

Journal of Hydrology

journal homepage: www.elsevier.com/locate/jhydrol

Research papers

Time-lapse ensemble-based electrical resistivity tomography to monitor water flow from managed aquifer recharge operations

Mauricio Arboleda-Zapata [a,b,1,*], Gordon Osterman [b], Xinyan Li [a,b], Salini Sasidharan [c], Helen E. Dahlke [a], Scott A. Bradford [b]

[a] Department of Land, Air, and Water Resources, University of California, Davis, USA
[b] Sustainable Agricultural Water Systems Unit, United States Department of Agriculture, Davis, CA, USA
[c] Department of Biological & Ecological Engineering, Oregon State University, Corvallis, USA

ARTICLE INFO

This manuscript was handled by Corrado Corradini, Editor-in-Chief, with the assistance of Nick Engdahl, Associate Editor

Keywords:
Central Valley of California
Manage aquifer recharge
Drywell
Time-lapse electrical resistivity tomography
Geostatistics
Model ensemble

ABSTRACT

Various managed aquifer recharge strategies, such as drywells, are being used in the California Central Valley (CCV) to replenish groundwater resources that have been depleted by over-pumping, especially during droughts. Drywell technology allows recharge water to bypass shallow impermeable layers and possible contaminated soils near the land surface. Understanding water flow in the vadose zone is crucial for assessing the performance of drywells regarding the amount of water that reaches the groundwater table and the fate of solutes. In this study, we demonstrate the applicability of time-lapse electrical resistivity tomography (TL-ERT) for imaging the water flow and subsequent aquifer recharge at a drywell site in the CCV with a thick (67–72 m) vadose zone. Additionally, TL-ERT results were compared to point-scale observations from a collocated monitoring well. To invert our TL-ERT data sets, geostatistical constraints were applied to favor layered models as expected due to the alluvial deposits in the study area. By considering different correlation lengths, an ensemble of resistivity model solutions was generated per time-step instead of a single model solution (as typically performed). Model differences between the mean model of the baseline data set and the models from the subsequent time steps allowed us to image the wetting front development until reaching the regional aquifer, a perched water table, and flush of salts that were otherwise not visible or blurred when using single model solutions from standard deterministic TL-ERT inversion approaches.

1. Introduction

Semi-arid regions such as the California Central Valley (CCV) rely on groundwater resources to sustain intensive agricultural activity in a semi-arid, Mediterranean climate (Dahlke et al., 2018). The excessive water extraction rates in the CCV have historically surpassed the natural recharge of the Central Valley alluvial aquifer, and the resulting groundwater overdraft has depleted the underlying aquifer leading to well failure, land subsidence, and the threat of basin closure (Galloway & Burbey, 2011; Liu et al., 2022; Jeanne et al., 2019). Managed aquifer recharge (MAR) strategies have been developed to replenish groundwater resources (Kocis & Dahlke, 2017; Dahlke et al., 2018; Dillon et al., 2019), using excess water from runoff and snowpack accumulated during wet winters, treated surface water, or reclaimed wastewater (Bouwer, 2002). MAR is commonly implemented by infiltrating water at the land surface in surface spreading basins, fallowed agricultural lands, and designated floodplains, or directly into the aquifer through aquifer storage and recovery (e.g., Ringleb et al., 2016). Increasing attention has focused on directly infiltrating water in the vadose zone, using techniques such as infiltration trenches or galleries, and drywells. Techniques such as drywells can bypass shallow, impermeable layers and modeling exercises indicate that they are capable of infiltrating comparable amounts of water to 70 m diameter surface spreading basin (Sasidharan et al., 2018,2020).

In the CCV, MAR techniques are seen as important tools for achieving state-mandated groundwater sustainability targets (California Department of Water Resources, 2014). However, quantifying the efficacy and efficiency of MAR operations remains a difficult task, as it requires practitioners to monitor spatiotemporal changes in vadose zone water storage, water table elevation, and contaminant transport (Perzan et al.,

* Corresponding author at: Department of Land, Air, and Water Resources, University of California, Davis, USA.
E-mail address: mauricio.arboleda-zapata@uni-tuebingen.de (M. Arboleda-Zapata).
[1] Now at the Department of Geosciences, University of Tübingen, Tübingen, Germany.

https://doi.org/10.1016/j.jhydrol.2025.133282
Received 18 October 2024; Received in revised form 29 March 2025; Accepted 8 April 2025
Available online 14 April 2025

2023). Water flow in the vadose zone is typically monitored using in-situ sensors such as tensiometers, water content sensors, and electrical conductivity probes installed in the root zone or in boreholes (e.g., Gvirtzman et al., 2008), which are often sparsely located due to time and budget constraints. Although such measurements can provide reliable point-scale data, it can be challenging to extrapolate these measurements to the scale necessary to understand water flow in heterogeneous vadose zone systems where the hydraulic conductivity may vary by several orders of magnitude (Daily et al., 1992; Park, 1998).

Geophysical techniques can image subsurface heterogeneities and water flow over large spatial scales. Electrical resistivity tomography (ERT) is sensitive to the resistivity of the subsurface, which is a spatial function of water content, salinity, sediment texture, and temperature (e.g., see Binley & Slater, 2020, for an overview). These properties can change over time, as expected in MAR operations. Therefore, time-lapse ERT (TL-ERT) can be a valuable tool for capturing such temporal changes while also providing estimates of hydraulic properties (Daily et al., 1992; Singha et al., 2015; Uhlemann et al., 2022). For example, previous studies have shown the applicability of TL-ERT to monitor water flow in irrigated crop fields (e.g., Michot et al., 2003; Ogunmokun & Wallach, 2021), wetlands (e.g., Musgrave & Binley, 2011; Uhlemann et al., 2016), coastal areas prone to seawater intrusion (e.g., de Franco et al., 2009; Palacios et al., 2020), mountain hillslopes (e.g., Miller et al., 2008; Pleasants et al., 2022; Uhlemann et al., 2024) including areas prone to landslides (Perrone et al., 2014; Whiteley et al., 2019), and in multiple well injections with tracer tests (e.g., Oldenborger et al., 2007; Müller et al., 2010; Lesparre et al., 2017).

Monitoring MAR operations with TL-ERT, however, has been studied little and has mainly focused on monitoring MAR projects from spreading basins. For example, Sendrós et al. (2020) used TL-ERT to monitor the recharge of two shallow aquifers (< 6 m deep) from two recharge basins that use pretreated wastewater. Haaken et al. (2016) used TL-ERT to monitor a recharge experiment over two weeks in an infiltration basin that uses reclaimed wastewater for recharge. Although their survey could resolve resistivity to 10 m depth, they were unable to image the infiltration front reaching the water table at a depth of 39 m. García-Menéndez et al. (2018) used TL-ERT to investigate a MAR operation in which fresh water was injected through wells directly into a brackish aquifer at depths between 50 and 95 m to improve water quality (conversely, flow mainly occurs vertically in the vadose zone during drywell MAR). These studies illustrate the potential of TL-ERT for monitoring water flow in infiltration basins and injection wells (that are screened below the water table level), but to our knowledge, TL-ERT has not been used to monitor drywell MAR operations, or recharge operations in thick vadose zone settings (>50 m) that, for example, are frequently found in the CCV. In addition, TL-ERT must be applied over longer durations to capture water flow behavior and recharge in deep vadose zones.

In this study, we demonstrate how TL-ERT can monitor drywell MAR operations in a geological context featuring a thick, heterogeneous vadose zone. TL-ERT surveys were conducted between March 2023 and February 2024, during intervals when intermittent water was injected into five drywells and after completely stopping water injections. A geophysical modeling approach was employed where ensembles of ERT resistivity models were used to characterize the subsurface (e.g., Yeh et al., 2002; Ramirez et al., 2005; Audebert et al., 2014; Arboleda-Zapata et al., 2022) instead of a single model solution, the most typical approach. By extending this approach to TL-ERT, we were able to characterize the likely resistivity structure of the subsurface, as well as quantify the spatiotemporal uncertainty in our models while reducing artifacts that frequently appear in TL-ERT models. The results from this study illuminated complex vadose zone flow dynamics between the drywells and the water table at a depth of approximately 67 to 72 m below land surface. By comparing the TL-ERT resistivity models with point sensor data in a co-located monitoring well, the TL-ERT models were qualitatively interpreted to understand the redistribution of water and salts in the subsurface and, crucially, after water injection from drywells stopped.

2. Study area

Our study area is located in the southern CCV, 30 km southwest of Fresno, CA, at Terranova Ranch (Fig. 1a). The CCV is a large, elongated alluvial basin of approximately 52,000 km^2, flanked by the Coast Ranges to the west and the Sierra Nevada Mountains to the east. The Valley subsurface is composed of Pliocene unconsolidated alluvial and lacustrine deposits, including intercalations of coarse (gravels and sands) and fine (silts and clays) materials (Faunt et al., 2010). The Mediterranean climate of the CCV provides ideal conditions for year-round production of a diverse range of crops, including almonds, walnuts, pistachios, tomatoes, grapes, and citrus fruits. Thus, the CCV is considered one of the most productive agricultural regions in the world (Faunt et al., 2010). However, the average annual precipitation in the CCV is relatively low and ranges from 250 to 500 mm, with the northern regions receiving more rainfall than the southern areas (Faunt et al., 2009). Therefore, groundwater is frequently used to support the intensive, year-round agricultural production of the CCV (Faunt et al., 2016). Extensive groundwater pumping has significantly lowered the groundwater table, with the extent of the decline unevenly distributed across the CCV. Well water level measurements made between 2013 and 2018 show that the water table depth rarely exceeds 30 m in the northern CCV, while in the southern CCV, the water table depth can exceed 100 m (Jasechko & Perrone, 2020). These groundwater level declines have led to subsidence rates of up to 0.25 m/year in certain areas of the CCV (Faunt et al., 2016; Jeanne et al., 2019; Kang & Knight, 2023) and caused many shallower wells, often used for domestic supply, to run dry (Jasechko & Perrone, 2020). Under these circumstances, MAR techniques have gained attention for their potential to alleviate the overdraft of aquifers and ensure the long-term sustainability of the CCV groundwater resources (e.g., Kocis & Dahlke, 2017; Dahlke et al., 2018; Levintal et al. 2023).

3. Manage aquifer recharge setup and monitoring

Our study area at Terranova Ranch is shown in Fig. 1b. MAR operations at Terranova in 2023 were conducted using five drywells in the agricultural field along the highway as well as in three fallowed agricultural fields (indicated as Flood-MAR in Fig. 1b). The water was sourced from flood flows from the Kings River during the historically wet hydrologic year of 2023 (California State Water Resources Control Board, 2023). In the agricultural fields, 90 ha were flooded with 1–2 m of water from April to August. While this certainly contributed a large amount of water for infiltration, an unknown amount was "lost" due to evaporation, and another portion was held in the vadose zone (i.e., water that cannot be recovered but could contribute to a more efficient infiltration in the next recharge season). Furthermore, surface spreading techniques over fallowed agricultural fields and orchards may leach contaminants from the root zone to the groundwater (Zhou et al., 2024).

3.1. Drywells

The five drywells (DW) installed at Terranova, DW1-DW5, are 1.2 m-diameter structures that consist of two primary components: an upper sedimentation chamber from the surface down to five meters depth, and an underlying permeable gravel-packed chamber installed to a depth of 16 m to 35 m depending on the drywell (see Table 1). These drywells release water from the gravel-packed chamber into the vadose zone under a high hydraulic head that can produce large infiltration rates (Edwards et al., 2016; Sasidharan et al., 2018). Additionally, these drywells allow shallow impermeable layers to be bypassed that would otherwise impede water flow toward the deep (67–72 m below land surface) groundwater table.

Water was piped from the canal located southwest of our ERT profile

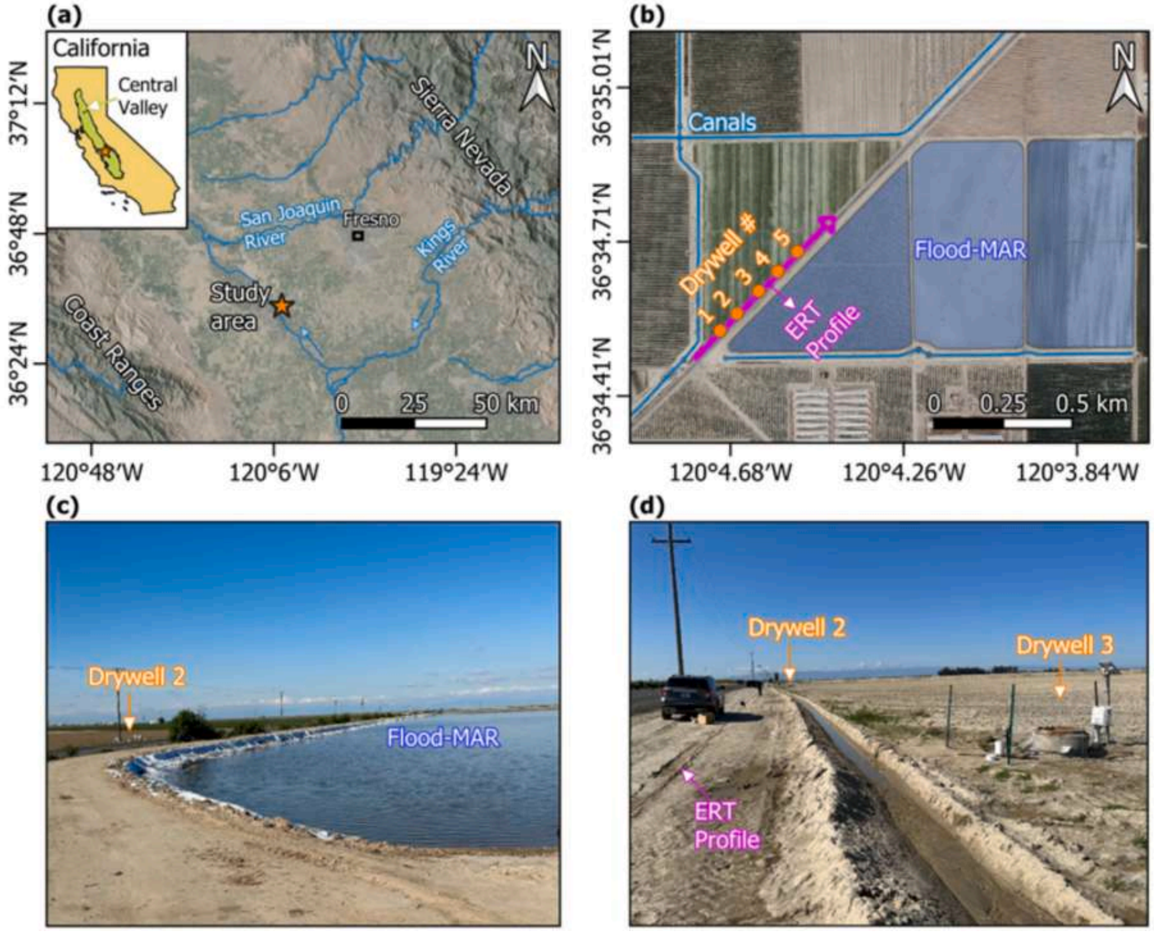

Fig. 1. Study area and experiment setup. (a) Regional overview of the study area, (b) details of our study area at the Terranova Ranch indicating the managed aquifer recharge setup (drywells and Flood-MAR) and the location of our ERT profile, where the first electrode is located at the southwest end of the magenta line. Photographs provide additional context at the flood-MAR fields (c) and the drywells (d) in our study area.

Table 1
Drywells depths and their relative distances from the position from the beginning of the ERT profile.

Drywell name	Depth range of gravel pack [m]	Distance along ERT profile [m]
DW1	5–27	135
DW2	5–16	222
DW3	5–28	335
DW4	5–35	433
DW5	5–26	534

(see Fig. 1b) to the sedimentation chamber of each drywell. Intermittent water flow to the drywells occurred from April 20, 2023, to July 31, 2024, by opening valves at the entrance of the canal and drywells. A geotextile membrane (Mirafi 140 N, White Cap) was installed at the canal entrance or at the entrance of the sedimentation chamber to reduce suspended sediment loads and the risk of clogging. When the water level in the sedimentation chamber reached a certain elevation, the water spilled into an overflow pipe leading to the bottom of the gravel-packed chamber, where it could infiltrate into the surrounding formation. The sedimentation chambers were instrumented with pressure transducers (CS451, Campbell Scientific) and turbidity sensors (Clarivue 10, Campbell Scientific) to determine water levels and the potential for clogging, respectively. The gravel-packed chamber had a water level sensor to monitor infiltration.

3.2. Monitoring well

A monitoring well was drilled within three meters of DW2, to a depth of 76.2 m using a sonic drilling rig. A sensor that measures electrical conductivity, temperature, and water content (Teros 12) was installed in the vadose zone of the monitoring well at depths of about 13.7, 21, 26.5, and 44.5 m (see Fig. 2). In this study, we report pore water conductivity estimated by the Teros 12 rather than bulk electrical conductivity because we are more interested in imaging potential solute transport processes (e.g., Müller et al., 2010) in the vadose zone related to our MAR operations. The pore water conductivity from the Teros 12 device is derived from measured bulk electrical conductivity and electrical permittivity, as indicated by Hilhorst (2000). Additionally, a water level sensor (CS451, Campbell Scientific) was placed at the bottom of the monitoring well. Teros data was recorded every 15 min, while water level data was logged every minute using a data logger.

The soil texture of core samples was determined in the field by hand and logged when differences in soil texture were observed. A simplified driller's log is shown in Fig. 2, where all layers are classified as either sandy or silty/clayey. The log indicates that the subsurface exhibits a high degree of vertical variability, where likely low permeability silty and clayey layers (brown) are intercalated with likely higher permeability sandy layers (yellow).

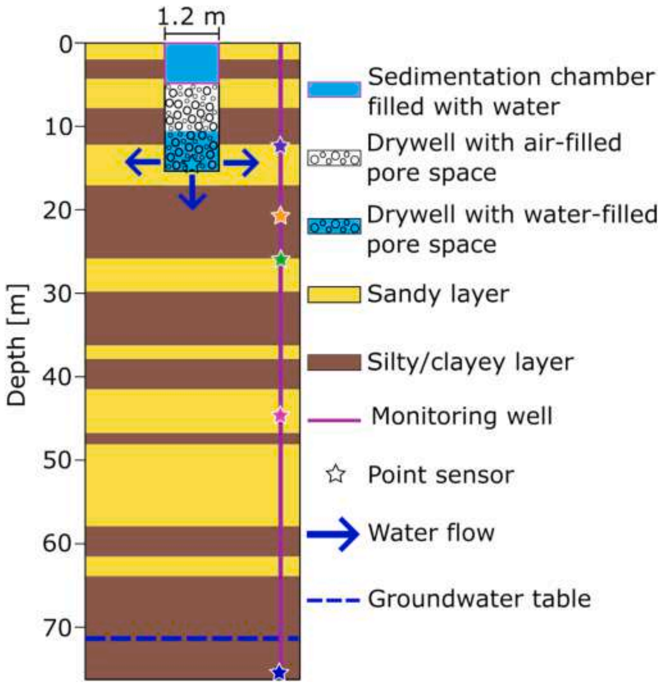

Fig. 2. Simplified geological log from the 76.2 m deep monitoring well (purple line) located within 3 m from drywell 2, which is sketched on the top of the figure. The point sensor positions are indicated with stars with the same color as the corresponding lines in Fig. 3. The water table given at ~71 m was recorded on April 20, 2023. Note that the horizontal axis is not to scale.

4. ERT

4.1. ERT background

ERT has been used for a wide range of vadose zone hydrogeological applications due to its sensitivity to sediment texture, water content, and pore fluid salinity (Singha et al., 2015). ERT (and other electromagnetic methods) image the subsurface electrical resistivity, which is the inverse of electrical conductivity (note, any time we refer to conductivity, we are referring to electrical conductivity; references to hydraulic conductivity will be explicitly spelled out). Increasing the water content will increase the number of electrically conductive pathways through a porous medium, thereby decreasing resistivity. Additionally, increasing the concentration of dissolved salts in the porewater will make the existing electrically connected pathways and porous medium less resistive (more conductive). Consequently, it can be difficult to separately monitor changes in water content and salinity in the vadose zone during a recharge experiment. One additional challenge is differentiating resistivity from clayey and sandy units under changing saturation conditions. Clay minerals have a larger cation exchange capacity, surface area, and water holding capacity than sands, resulting in clays having a higher surface conductivity and, conversely, lower resistivity than sands. For example, in the context of a wetting front moving through the vadose zone (as in a MAR scenario), the resistivity of clayey and sandy units might be modified by different degrees of magnitude (for example, due to differences in hydraulic conductivity, and water storage and holding capacities), and the recovery time to initial conditions might vary significantly.

Standard 2D ERT data acquisition is described in detail by Binley and Slater (2020), and a brief overview is given here. During an ERT experiment, a known electrical current is injected into the ground through a pair of stainless-steel electrodes inserted into the ground while the resulting voltage is recorded in another pair of electrodes, where the measurement across the specific combination of four electrodes is referred to as a quadrupole. The ratio between the measured voltage and the injected current multiplied by a geometric factor that accounts for the relative position of the electrodes gives the apparent resistivity, i.e., the resistivity corresponding to a hypothetical, uniform half-space. By systematically changing the quadrupole geometry along the array, a set of apparent resistivities with varying spatial sensitivities can be obtained.

To quantify measurement error, measurements at quadrupoles should be repeated—or stacked. Measurements using the standard quadrupole geometry are referred to as normal or forward measurements, while measurements where the current injection and voltage measurement electrodes are swapped, the measurements are referred to as reciprocal or reverse measurements. According to the reciprocity principle, the electrical response, and thus the spatial sensitivities, of forward and reciprocal measurements are identical, assuming an ideal scenario without any noise source. Thus, the deviation between forward and reciprocal measurements can be used to quantify systemic errors that standard stacking would not pick up (Zhou & Dahlin, 2003).

The measured apparent resistivity data does not describe an accurate model of the subsurface. Thus, the objective of ERT data inversion is to reconstruct plausible subsurface resistivity models that explain the measured data within the constraints of the assumed data error estimates and prior knowledge. During ERT data inversion, we aim to recover a resistivity model $\mathbf{m}$ that minimizes the cost function Φ:

$$\Phi(\mathbf{m}) = \|\mathbf{C}_{\mathrm{D}}^{-0.5}(\mathbf{d} - f(\mathbf{m}))\|_2^2 + \lambda\|\mathbf{C}_{\mathrm{M}}^{-0.5}(\mathbf{m} - \mathbf{m}^{ref})\|_2^2 \tag{1}$$

Here, the first term quantifies the data misfit, measuring the difference between observed data $\mathbf{d}$ and predicted data (i.e., a forward operator f applied to model $\mathbf{m}$), using the squared L2-norm (note the superscript and subscript in the norm) and incorporating data constraints through the diagonal matrix $\mathbf{C}_{\mathrm{D}}$ whose non-zero elements are equal to the inverse of the estimated/assumed data errors (i.e., assuming an uncorrelated Gaussian noise distribution). The second term represents the model misfit, which quantifies the deviation of the model $\mathbf{m}$ from a reference model $\mathbf{m}^{ref}$, using the squared L2-norm and incorporating prior constraints through the covariance matrix $\mathbf{C}_{\mathrm{M}}$. Finally, λ represents the model regularization parameter that controls the trade-off between minimizing the data and model misfit terms. Typically, the error level is estimated (e.g., from reciprocal errors) or assumed (e.g., user-defined Gaussian distribution). Such weights can strongly influence the reliability of the inverted resistivity models (e.g., Labrecque et al., 1996; Slater et al., 2000; Koestel et al., 2008; Tso et al., 2017). Additionally, the reference model is typically assumed to be the same as the starting model, which is generally assumed to be homogeneous. It is important to note that the matrix $\mathbf{C}_{\mathrm{M}}$ can be used to include prior knowledge about the subsurface, such as geological features, expected resistivity distributions, and spatial correlations (e.g., Hermans et al., 2012; Jordi et al., 2018; Grünenbaum et al., 2023). By incorporating such prior information as a weighting matrix, it can help to guide the inversion toward more geologically plausible solutions, even when the data alone may be insufficient to constrain the model fully. Caterina et al. (2014) provide some general examples of constrained deterministic inversion approaches commonly used to invert ERT data. In this study, all inversions were performed using a deterministic approach in the open-source software pyGIMLi (Rücker et al., 2017).

Monitoring transient subsurface processes such as MAR operations requires collecting ERT data sets at different time steps (i.e., TL-ERT). There are four common approaches to recovering TL-ERT resistivity models. The first approach consists of individually inverting ERT data for each time step and subsequently calculating model differences between the inverted models. Some studies have shown that this approach can result in unrealistic resistivity changes (e.g., Miller et al., 2008; Loke et al., 2022; Johnson et al., 2015), also referred to as time-lapse model artifacts. The second approach consists of using a baseline model (e.g., the model obtained after inverting the first data set) as the reference or starting model for the inversion of ERT data sets at subsequent time steps

(Miller et al., 2008; Audebert et al., 2014; Dietrich et al., 2018). The third approach involves inverting the ratio or difference between two ERT data sets (e.g., Daily et al., 1992; Park, 1998; Slater et al., 2000; LaBrecque & Yang, 2001). While the second and third approaches can smooth out time-lapse artifacts visible in the first approach, they can generate their own anomalous artifacts, due to, for example, varying noise levels and complex resistivity changes at each time step (e.g., Lesparre et al., 2017). Finally, the fourth approach involves methods that impose smoothness constraints over time by considering all time steps or a subset (e.g., Kim et al., 2013; Wilkinson et al., 2022). This approach seems to produce more stable solutions over time than the previously described three approaches. However, like the other three approaches, it provides limited insights into model uncertainties due to the non-uniqueness of the inverse problem.

An alternative approach that can produce more stable model solutions across time while also providing uncertainty estimates is to recover an ensemble of models at each time step and calculate the main trend (e.g., mean or median) between the ensembles to estimate model differences (e.g., Ramirez et al., 2005). Because the ERT inverse problem is highly non-unique, exploring the whole model solution space can be computationally prohibitive. Therefore, prior information can be included in the regularization term of Eq. (1) to constrain the number of possible solutions. For example, alluvial systems such as those observed in the CCV can be described in terms of their spatial correlation structure (e.g., Gelhar, 1993; Tronicke & Holliger, 2005). It is possible to incorporate this geostatistical information into the regularization following the framework proposed by Jordi et al. (2018), which is implemented in the software pyGIMLi. This framework creates geostatistical regularization operators based on an exponential covariance model that considers distances extending beyond neighboring cells. The maximum distance over which one cell might have an influence over another cell is commonly named correlation length. Such regularization operator carries the a priori geological information that will be used to weight the model misfit term in Eq. (1). The relative influence of such a geostatistical operator is additionally weighted by λ. A larger λ might result in models with correlation lengths closer to the a priori correlation lengths. Otherwise, by setting a small λ value, we might favor results based on the data misfit term of Eq. (1), and the resulting correlation length might differ significantly from a priori correlation lengths. Examples showing the applicability of such an approach to study layered alluvial systems are presented by Palacios et al. (2020) and Arboleda-Zapata et al. (2023).

One of the main challenges when inverting ERT data using geostatistical constraints is determining which vertical (C_z) and horizontal (C_x) correlation lengths are most appropriate for obtaining resistivity models in agreement with plausible geological models. Although well-log information can narrow down the plausible range of correlation length scales, it is important to note that the correlation lengths of an ERT model do not perfectly match those of the local hydrogeology. Rather, the recovered ERT model depends on the data, which is subject to the resolution limitations of the ERT method, the assumed prior model, and the regularization scheme employed (e.g., Hermans & Irving, 2017). Therefore, following Jordi et al. (2018) and Arboleda-Zapata et al. (2023), it is best to invert ERT data considering a range of different correlation lengths. This will provide a simple means of systematically generating an ensemble of model solutions at each time step. One advantage of this approach is that descriptive statistics such as the mean resistivity of an ensemble of model solutions highlight consistent features across the ensemble, minimizing the impact of artifacts isolated to a specific set of regularization parameters (e.g., Hermans et al., 2012; Pereira et al., 2023). Importantly, it is easy to perform an uncertainty analysis on such an ensemble of models to identify what parts of the resistivity model are well resolved.

4.2. TL-ERT data acquisition

To monitor the temporal evolution of water content following water injection through the five drywells at Terranova, 11 ERT data sets (ERT0, ERT1, …, ERT10) were collected along the profile parallel to the drywells shown in Fig. 1b. These data were collected from March 2023 until February 2024, with more frequent data acquisition just after the start of water injection in April 2023 (see Fig. 3). To collect these TL-ERT data sets, we used 96 stainless-steel electrodes spaced every 5 m and performed a 48-electrode roll-along, resulting in a 715 m-long profile. Note that our profile extends 135 m past DW1 and 181 m past DW5 (see Table 1) to ensure adequate sensitivity below all our drywells where we expect the added water to most significantly alter the electrical resistivity of the subsurface. Depending on system availability, we used either a Syscal Terra (ERT0-ERT1, ERT7-ERT10) or a Syscal Pro device (ERT2-ERT6), both from IRIS Instruments (Orleans, France).

To measure the apparent resistivities, we used the multi-gradient and dipole–dipole array configurations with a fixed voltage of 100 V and a measurement duration of 0.5 s. The array configurations were selected to provide complementary zones of sensitivities to better constrain the resulting resistivity model (e.g., Comte et al., 2012). Multigradient and dipole–dipole array configurations are optimized for multi-channel data acquisition, which allowed us to acquire data very rapidly. Further details regarding the sensitivity distributions, advantages, and limitations of these array configurations can be found in Stummer et al. (2004), Furman et al. (2003), and Audebert et al. (2014).

For all time steps, we acquired 2–4 stacks, using only 2 if the standard deviation was below 3 %, and 4 if it exceeded this threshold. The Syscal Terra data generally exhibited lower errors than the Syscal Pro; however, both systems provided high-quality data with standard deviations lower than three percent for most of the measurements. In the end, the reported apparent resistivity and observed error were calculated as the mean and the standard deviation across the repeated measurements at each quadrupole, respectively. Additionally, we collected reciprocal data for about 25 % of our quadrupoles. We quality-controlled the ERT data by setting the stacking error and reciprocal error thresholds to 5 % and 10 %, respectively. Where we had collocated forward and reciprocal measurements, we averaged them unless the relative difference between the two measurements exceeded 30 %, in which case we removed the measurement with the higher stacking error.

4.3. TL-ERT data inversion

To invert our ERT data, we systematically varied the parameters of the regularization term in Eq. (1) by considering the geostatistical framework from Jordi et al. (2018) that was briefly outlined in Section 4.1. To implement our geostatistical regularization, we used a range of lateral correlation length scales (C_x) and vertical correlation length scales (C_z) given in Table 2. In the layered sedimentary environment of the CCV, we expect the primary correlation axes to be in horizontal and vertical directions, so we set the rotation angle to zero. In the end, this results in an ensemble $\mathbf{M}$ consisting of 216 resistivity model solutions at each time. In this study, we use the mean resistivity and standard deviation at each inversion cell to summarize the general trend and variabilities for the obtained ensembles for each time step.

By inverting the initial (baseline) ERT data set at time step T_0, we obtain the baseline model ensemble $\mathbf{M}^{T_0}$. Then, by inverting the k subsequent ERT data sets at time steps $T_1, T_2, \dots, T_k$, we obtain the model ensembles $\mathbf{M}^{T_1}, \mathbf{M}^{T_2}, \dots, \mathbf{M}^{T_k}$. To summarize the differences between $\mathbf{M}^{T_k}$ and $\mathbf{M}^{T_0}$, we evaluated the difference between their mean models ($\mathbf{m_d}$) as follows:

$$\mathbf{m}_\mathrm{d} = \frac{\overline{\mathbf{M}}^{T_k} - \overline{\mathbf{M}}^{T_0}}{\overline{\mathbf{M}}^{T_0}}. \quad T_k > 0 \tag{2}$$

In addition to comparing the mean models, we calculated the relative

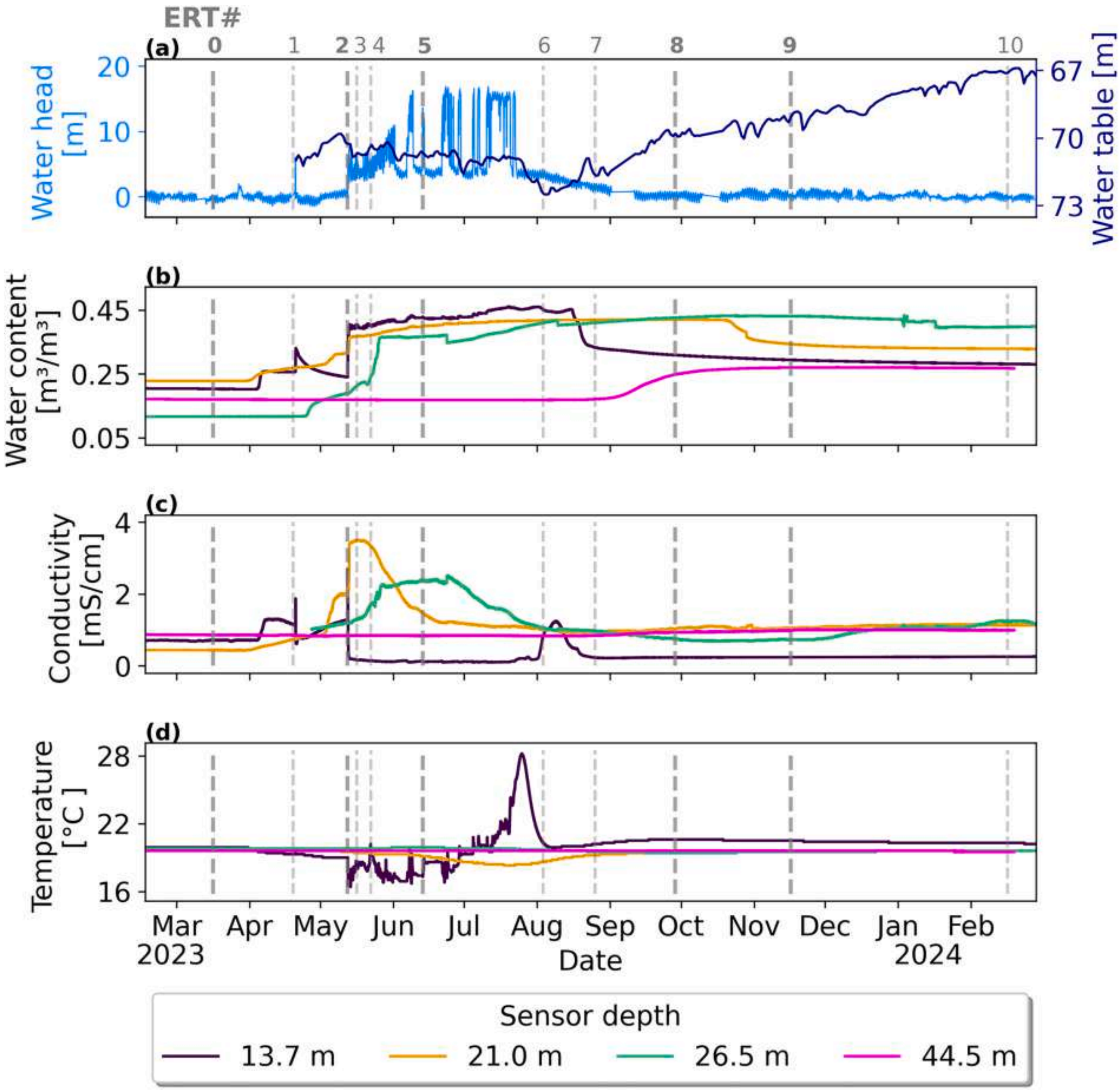

Fig. 3. Point sensor measurements. (a) Water head (left axis) estimated from a pressure sensor located at the bottom of the gravel-packed chamber of DW2, and water table depth below the ground surface (right axis) estimated from a level sensor placed at the bottom of the monitoring well. Monitoring well data of (b) water content, (c) pore fluid electrical conductivity, and (c) temperature at 13.7, 21.0, 26.5, and 44.5 m depth. The vertical gray dashed lines in panels (a)-(d) indicate the time when ERT data sets were collected. Bold gray indexes on top of panel (a) and thicker gray lines highlight the ERT time steps shown and discussed later in this manuscript. Results from the other time steps are presented as supporting information (S1-S4).

Table 2
Trade-off and geostatistical regularization parameters used to invert ERT data at all time steps.

Inversion Parameters	Values
Regularization parameter (λ)	1, 5, 10, 20, 40, 80, 160, 320, 640
Horizontal correlation lengths (C_x) [m]	20, 40, 80, 160, 320, 640
Vertical correlation lengths (C_z) [m]	2, 4, 8, 16

differences between the model solutions obtained using the same inversion parameters for ensembles at times T_k and T_0. Assuming that the models at index j for each ensemble consisting of n models were obtained using identical inversion parameters, we evaluated the model differences $\mathbf{M}_\mathrm{d}$ as follows:

$$\mathbf{M}_\mathrm{d} = \frac{\mathbf{M}_j^{T_k} - \mathbf{M}_j^{T_0}}{\mathbf{M}_j^{T_0}}. \quad T_k > 0 \tag{3}$$

For our inversions, we considered homogeneous starting and reference models equal to the mean apparent resistivities, ranging from 75 to 98 Ωm, for the corresponding TL-ERT data set. Inversions were conducted on a triangular mesh composed of two regions, a core model extending from X = −10 until X = 725 m and from the surface to a depth of 80 m, and an appended, coarser mesh that extends beyond the core model domain to avoid numerical imprecision (Rücker et al., 2006). The mesh was built to have two elements between electrodes resulting in 4891 cells in the core mesh, and a total of 6649 cells across the entire domain.

As mentioned in Section 4.1, the assumed error model has a large influence on the resulting model. Therefore, before creating our ensembles of models we ran some preliminary tests where error estimates were derived from repeated measurements, Gaussian error estimates as implemented in pyGIMLi (Günther et al., 2006), and reciprocal errors as described by Blanchy et al. (2020). However, inversion results using these error estimates produced data residual distributions with noticeable structural correlation and anomalously high values. Consequently, we examine various customized strategies that enhance performance by reducing the correlation of data residuals and minimizing overall data misfit.

The final error estimates implemented in this study used a hybrid approach that consisted of three main steps. In the first step, we created two random vectors from a lognormal distribution of the same size as our ERT data set with minimum and maximum values of 0.001 and 0.03, respectively, to simulate our expected error levels based on our repeated and reciprocal data errors. The first error vector ε_k was sorted such that the error scaled with geometric factor. Similarly, the second error vector ε_ρ was sorted so that the error scaled with resistivity. In the end, our error estimate ε is calculated as:

$$\varepsilon = \alpha\varepsilon_k + (1-\alpha)\varepsilon_\rho,\ 0 < \alpha < 1, \tag{4}$$

where α is a trade-off parameter between the two terms of the equation. In this study, we tested α values of 0.25, 0.5, and 0.75. We observed no significant differences and set $\alpha = 0.5$ for all time lapses. It is important to note that setting $\alpha = 0.5$ indicates that the geometric factors and apparent resistivity values influence our error calculations equally.

5. Results

5.1. Point sensor measurements

Fig. 3 shows measurements from drywell DW2 and the monitoring well. We report the water head level in the gravel-packed chamber of DW2 (Fig. 3a, left axis), and for the monitoring well, we report the water table depth below the ground surface (Fig. 3a, right axis), water content (Fig. 3b), estimated pore fluid conductivity (Fig. 3c), and temperature (Fig. 3d). Note that in Fig. 3b–d, the measurements are reported for four different depth intervals. Vertical gray dashed lines indicate the ERT data acquisition times. In Fig. 3a, head levels of 0 m and 16 m correspond to the empty and full conditions in DW2, respectively. There was an initial pulse of water in April 2023, but the drywells were not fully turned on until mid-May 2023. We can see the intermittent injections running from May 2023 through the end of July 2023, after which the head dropped from a maximum of 16 m to approximately 5 m within a couple of days, but it took another 40 days for the head to drop to 0 m.

In response to the primary pulse on April 19 (Fig. 3a), we observe a large jump in water content (Fig. 3b) in the ports at 13.7 m and 21.0 m starting at approximately 0.2–0.25 m^3/m^3 in early April and exceeding 0.4 m^3/m^3 over the summer of 2023. Although water deliveries to the drywells stopped at the end of July, water content in the 13.7 m port did not start decreasing until mid-August, and not until mid-October for the 21.0 m port. However, the pulse takes longer to reach 26.5 m, arriving in late May 2023, and not reaching a maximum of around 0.45 m^3/m^3 until around October through November. The deepest port at 44.5 m does not see an increase in water content until mid-September 2023, only rising to approximately 0.25 m^3/m^3 and never decreasing in the timeframe studied.

Consequently, the average vertical migration rate from DW2 was initially very rapid, but this rate decreased with depth after water release from DW2 stopped. The average water migration rate over the five-month period between 16 m (the bottom of DW2) and 45 m depth was about 0.2 m/day (i.e., the wetting front traveled about 30 m in 5 months). It is important to emphasize that the water table (Fig. 3a, right axis) shows recovery from August 2023 through February 2024. At first, this seems to contradict the data from our port at 44.5 m, which suggests that the wetting front does not arrive until mid-September. Consequently, a logical question arises: To what extent is this gradual rise in the water table due to direct recharge from our MAR experiment, and to what extent is it due to reduced pumping and regional recharge during the historically wet hydrologic year of 2023 (California State Water Resources Control Board, 2023)? We cannot answer this question using only point sensor data alone, but the TL-ERT results can provide further insights to help us determine the actual migration of the wetting front through the vadose zone until reaching the water table.

The measured pore fluid conductivity (Fig. 3c) follows different patterns than the water content. All ports show a background conductivity in the range of 0.5 mS/cm–1 mS/cm. After a very short spike starting in mid April, the conductivity at the 13.6 m port drops, while the conductivity in the 21.0 m port increases starting in early May from approximately 0.8 mS/cm to 3.5 mS/cm, but begins to decrease soon after, reaching a constant value of 1 mS/cm around July 2023. At the 26.5 m port, we observe a more gradual increase in conductivity that only reaches 2.5 mS/cm from mid-May to mid-June before decreasing to a steady-state value of about 0.8 mS/cm by August 2023. No meaningful change in conductivity is observed in the 44.5 m port throughout the entire experiment, even when the water content increases.

The starting temperature in all ports is about 20 °C and remained relatively stable at the time of the ERT experiments (Fig. 3d). We only observe meaningful temperature variations in the 13.7 m port, which initially decreases by approximately 3 °C with the arrival of the wetting front. There is an anomalous and brief increase in temperature to 28 °C after the water is shut off in mid July 2023 that reverts to the background temperature by early August. Otherwise, we only observe a small decrease in temperature in the 21.0 m port, and almost no variation in the two deepest ports. Temperature changes can be a useful indicator of the progression of a wetting front and can also be used to correct TL-ERT models when significant temperature changes occur (e.g., Hayley et al., 2010; Hermans et al., 2014). However, we do not expect the variations observed at the 13.7 m port to significantly impact the measured apparent resistivities—at least not to the extent that changes in saturation and salinity will. Additionally, performing temperature corrections for pulsed injections at discrete locations would require more extensive subsurface temperature measurements, which we do not have available.

5.2. TL-ERT models

5.2.1. TL-ERT models using a traditional approach

In Fig. 4a–e, we show the TL-ERT inversion results obtained using the second time-lapse approach described in Section 4.1, where the baseline model (ERT0, Fig. 4a) is used as a reference model to constrain model differences for subsequent time steps (e.g., Miller et al., 2008). Overall, these models exhibit a layered structure for the first 25 m, mainly characterized by high resistivity values. However, below 25 m these models primarily feature a thick, low-resistivity layer that extends to the bottom of the profile, occasionally exhibiting small semicircular patches of intermediate resistivity values (mainly near the bottom of the profile). The low-resistivity layer below 25 m gradually decreases in resistivity over time toward the end of the profile. For example, past DW5 at depths between 30 and 50 m, the resistivity values on May 12 (ERT2) are intermediate, while between June 13 (ERT5) and November 16 (ERT9), they show a noticeable decrease in resistivity.

In Fig. 4f–j, we show the relative resistivity changes between the time-lapse models and the baseline model. On March 16 (ERT1–ERT0), the changes are minimal but become more noticeable over time. For example, on May 12 (ERT2–ERT0), there are significant negative changes between 25 and 50 m. This negative layer gradually shifts downward, partially reaching the bottom of the profile on September 28 (ERT8–ERT0) and entirely on November 16 (ERT9–ERT0). As this negative layer descends, it leaves behind a layer of positive changes that thickens over time.

Overall, we observe significant discrepancies between results from the traditional approach with the available information, particularly at depths greater than 30 m where the resulting resistivity models are heavily smoothed. For example, note how the coarse dominant section

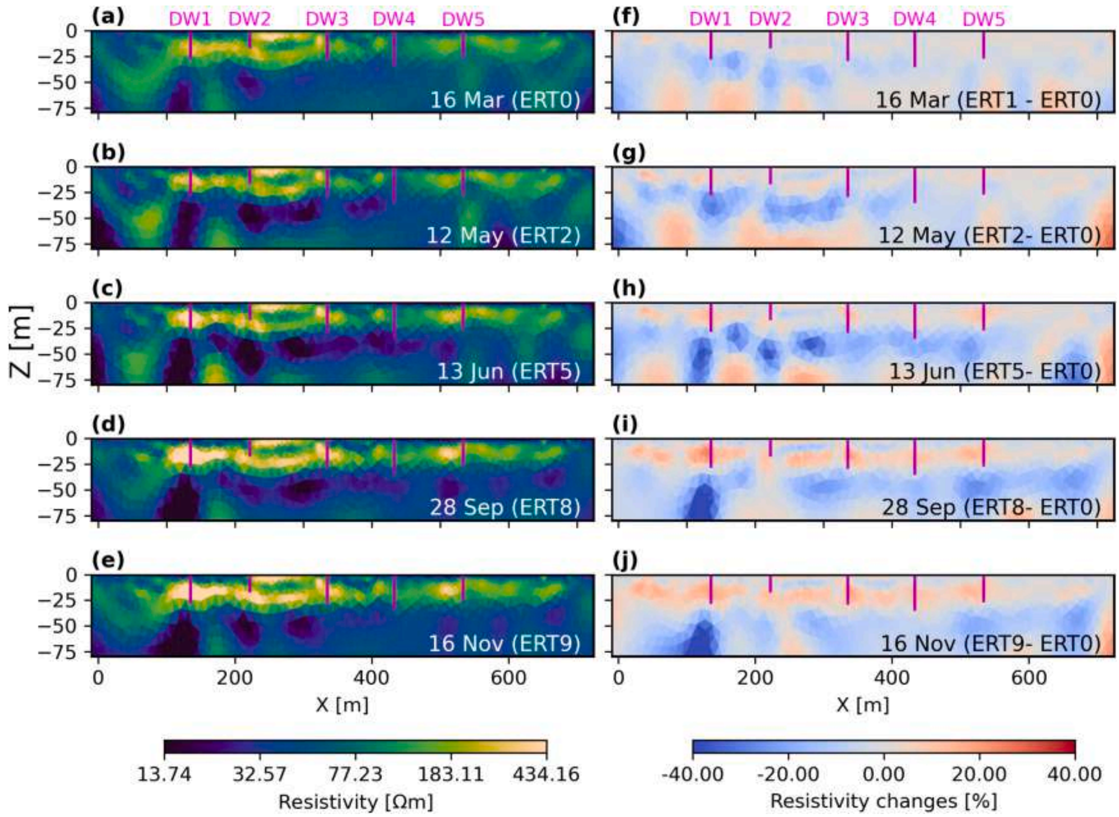

Fig. 4. TL-ERT results using single model solutions where the baseline model (ERT0) is used as a reference model to constrain model differences for subsequent time steps. Panels (a)–(e) correspond to the inverted resistivity models, and panels (f)–(j) correspond to the model differences with respect to the baseline model. The survey dates are given in the lower right corner of each panel. Drywell locations are indicated as magenta vertical lines. Results for all time lapses using this approach are presented in Fig. S1.

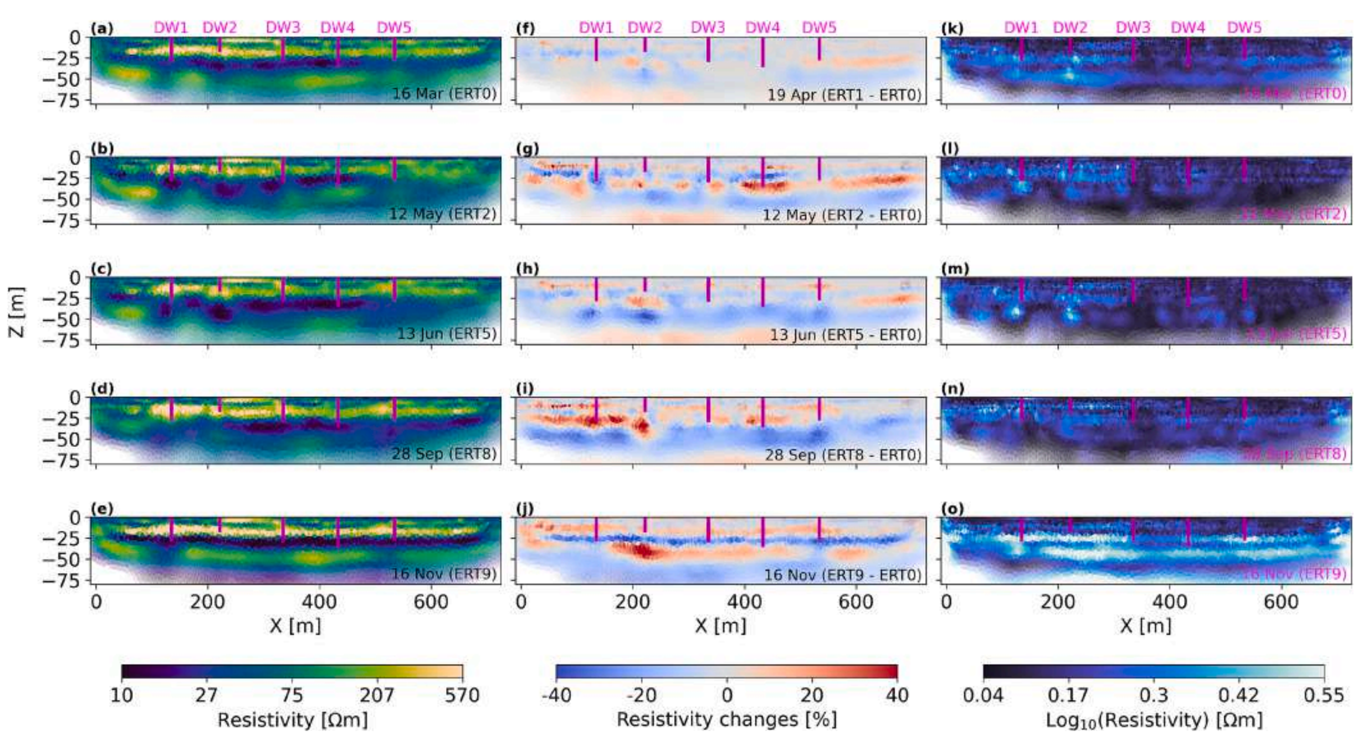

Fig. 5. Inversion results of our TL-ERT data sets using our ensemble approach. The panels (a–e) show the mean of the model ensembles, (f–j) the mean difference from Eq. (2), and (k–o) the standard deviation of model ensembles. The survey dates are given in the lower right corner of each panel. Drywell locations are indicated as magenta vertical lines. The mean and standard deviation for all model ensembles and the mean model differences are shown in Figs. S2 and S3, respectively.

between 35 and 60 m (see Fig. 2) exhibits relatively low resistivity values in ERT0 while we were expecting high resistivity values. Such discrepancies can significantly impact subsequent time steps, as their reliability depends on the accuracy of the baseline model (for this particular time-lapse approach). Therefore, the differences between the models are also overly smoothed, leading to discrepancies when compared to the point-scale sensor measurements shown in Fig. 3. For example, water content measurements suggest the presence of a perched layer at approximately 26 m depth, where water content remains at its peak of 0.45 m^3/m^3 since mid-August without decreasing. This perched layer should manifest in the model differences as negative resistivity changes. However, such changes are absent in the model differences from September 28 (ERT8–ERT0) and November 16 (ERT9–ERT0). Finally, a significant limitation of the traditional approach is the absence of uncertainty estimates for both resistivity values and their temporal changes.

5.2.2. TL-ERT models using the proposed ensemble approach

Fig. 5a–e show the mean resistivity model at selected time steps across the experiment with a transparency mask applied to areas with low sensitivity, primarily seen at depth and at the lower edges of the model. Note that each ensemble was generated by independently inverting each data set, i.e., no time constraints are considered. Overall, the mean models are characterized by a horizontally layered resistivity structure, roughly comparable to the structure observed in the models obtained with the employed traditional approach (see Fig. 4a–e).

When comparing the baseline models from the traditional and ensemble approaches (Figs. 4a and 5a, respectively), we observe that the traditional method fails to detect the low-resistivity layer centered at a depth of 35 m, as well as the underlying high-resistivity layer centered at a depth of 50 m. While we cannot state that the ensemble baseline model is correct, it aligns with the geological log presented in Fig. 2 better than the baseline model obtained with the traditional approach. These discrepancies between the baseline models may be a significant reason for the pronounced differences observed in the subsequent time steps, especially at depths below 25 m, where we observe a notably greater thickness of the resistivity layers from the models obtained using the traditional approach compared to the mean models.

For all our model solutions, we calculated the correlation lengths using the Python library GSTools (Müller et al., 2022). The obtained mean and standard deviation of the correlation lengths for all models together was 72 ± 15 m in the horizontal direction and 7.3 ± 1.3 m in the vertical direction, giving a vertical-to-horizontal correlation length scale ratio for the final model ensembles of approximately 0.1, which is typical for alluvial systems such as the CCV (Gelhar, 1993; Tronicke & Holliger, 2005). For comparison, we calculated the vertical correlation length of the driller's log in Fig. 2 by calculating the indicator variogram and fitting stable and exponential geostatistical models (Müller et al., 2022). These variogram models gave vertical correlation lengths of approximately 5 m, only slightly lower than the vertical correlation lengths of the resistivity model ensembles.

In Fig. 5f–j, we show the mean model differences between our background model and the models at subsequent time steps as calculated using Eq. (2). In Fig. 5f (ERT1–ERT0), we see the resistivity change after a very short injection, and there are correspondingly only small changes in subsurface resistivity. In Fig. 5g (ERT2–ERT0), after the longer injection began, we observe much larger changes in resistivity, including an expected decrease in resistivity around DW1 but more complex behavior around DW4, including an increase in resistivity around 40 m depth. This increase in resistivity is intermittently visible across the entire domain. Around 50 m depth across the model, we observe a general decrease in resistivity in ERT2–ERT0. In Fig. 5h (ERT5–ERT0), we see a broad decrease in resistivity at most drywells, although there are still some patches of increasing resistivity, such as the intermittent layers at 10 and 30 m depth, respectively. In Fig. 5i (ERT8–ERT0), we still observe a decrease in resistivity below 40 m across much of the profile, but we also see increases in resistivity, especially at DW1, DW2, and DW4, and the increase in resistivity at 10 m depth becomes more prominent. Finally, in Fig. 5j (ERT9–ERT0), we see a highly layered structure across the entire domain. Resistivity at 15–25 m depth is increasing, while from 25 to 35 m, we observe a substantial decrease in resistivity. From 35 to 50 m depth, the resistivity appears to increase between DW1 and DW5. The deepest layer below 50 m also shows a decrease in resistivity, whereas, in all previous time steps, we observed a minor increase in resistivity. Note, however, that these only show the differences of the mean models, which are used for illustrative purposes. We also need to look at how the ensembles vary over time.

In Fig. 5k–o, we show the standard deviation at selected time steps across the experiment. Generally, zones with high standard deviation tend to increase with depth, a common effect of decreasing model resolution as the distance from the electrodes increases (e.g., Hermans et al., 2012). This trend is particularly evident in Fig. 5k and 5o (ERT0 and ERT9, respectively), where two relatively thick zones with high standard deviation are centered at depths of 20 m and 45 m, with the deeper zone being significantly thicker than the shallower one. Additionally, it is worth noting that the zones with higher standard deviation mainly correspond to the layer interfaces in the mean model. For example, in Fig. 5a (ERT0), at about 25 m, there is an interface between a high and low resistivity layer, which corresponds to higher standard deviations. This suggests that the depths of the interfaces between these layers are uncertain. Kang et al. (2021) found similar results when analyzing ensembles of resistivity models from transient electromagnetic surveys. Additionally, by comparing the standard deviation at all time steps, we observe that Fig. 5o (ERT9) exhibits larger standard deviations below 20 m compared to previous time steps. We hypothesize that it may be a result of a combination of factors, including variations in electromagnetic noise associated with the parallel power line (see Fig. 1c and d), changes in the coupling of the electrodes to the ground, and limitations of our error model. Furthermore, note that the standard deviation tends to be higher in the initial section of the profile before DW3. This aligns with the higher contact resistance observed in this part of the profile and the presence of a couple of transformers along the parallel power line.

Fig. 6a and g show the geological log from Figs. 2, and 6b–f and h–l show vertical profiles (adjacent to the monitoring well at X = 222 m) of the ensembles of resistivity models and the ensemble of resistivity changes calculated using Eq. (3), respectively. Note that the mean value at each depth interval is also shown in all panels. In general, we observe in Fig. 6b–f low resistivity variance in the top 20 m across all time steps. However, below 20 m depth, the model variability generally increases with depth to around 60 m before the models re-converge. Overall, models for each time step depict similar structures but different amplitudes in resistivity. For example, in the 35–60 m depth interval in Fig. 6f (ERT9), many models exhibit resistivities above 200 Ωm, while others show values below 100 Ωm. This explains the high standard deviation observed at these depths in Fig. 5o, where uncertainty in resistivity is particularly pronounced.

In Fig. 6b (ERT0), although we do not see a precise correspondence between our binary sediment texture classification and the resistivity model, the main overall structure is retained. For example, the dip in resistivity between 30 and 40 m depth corresponds to a zone with more fine-dominated sediments, while the higher resistivity portion between 40 and 60 m corresponds to a zone with more coarse-dominated sediments. However, the main mismatch is observed at depths between 18 and 25 m, where a fine-rich layer shows resistivity values larger than expected. This is because the ERT array deployed, with 5 m electrode spacing, is not sensitive to thin sedimentary units in a complex alluvial system, especially at depth (Hermans & Irving, 2017).

The evolution of profiles in resistivity and resistivity changes over time provides valuable insights into subsurface processes. For example, the low resistivity peak centered at a depth of about 35 m in Fig. 6b

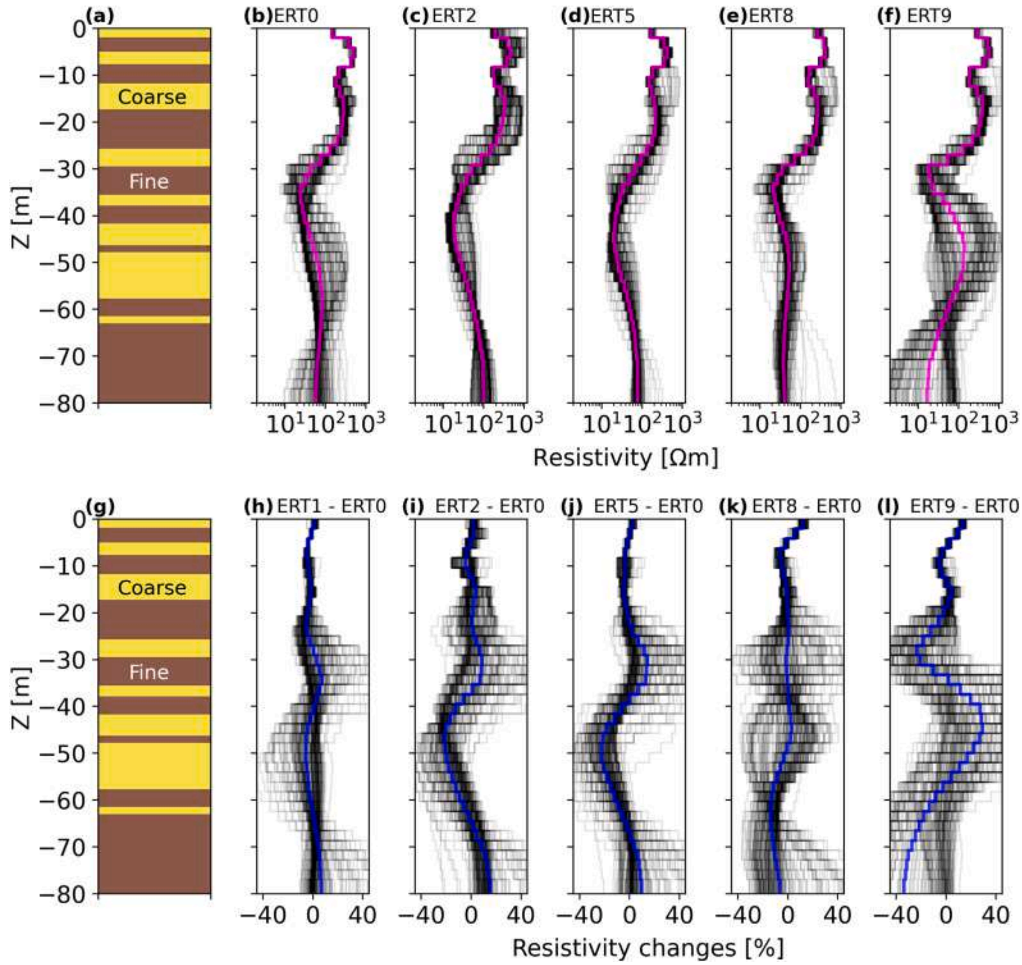

Fig. 6. Vertical profiles at the monitoring well (222 m along the profile). Panels (a) and (g) correspond to the geological log from the monitoring well next to DW2. Panels (b)–(f) are the vertical resistivity profiles at time steps (b) ERT0 (March 16), (c) ERT2 (May 12), (d) ERT5 (June 13), (e) ERT8 (September 28), and (f) ERT9 (28 September). Panels (h)–(l) are the vertical resistivity changes with respect to ERT0 for models obtained with the same inversion parameters (see Eq. (3) for (h) ERT1, (i) ERT2, (j) ERT5, (k) ERT8, and (l) ERT9. In panels (b)–(f) and (h)–(l), the magenta lines represent the mean resistivity, while the blue lines indicate the mean value of the resistivity changes at each depth. The black lines in panels (b)–(f) and (h)–(l) are plotted with transparency, so the darker areas indicate a higher density of vertical profiles.

gradually shifts downward from March 16 to June 13 (Fig. 6c and d), where the center of the peak is found at depths of 40 and 45 m, respectively. Note that this results in negative resistivity changes in Fig. 6i and j. Such vertical resistivity shifts might be illustrative of a passing wetting front. On September 28 (Fig. 6e), the low resistivity peak is not as evident as in the previous time steps, but there is still an overall decrease in resistivity below 50 m depth (Fig. 6k). On the other hand, a pronounced increase in resistivity is evident on November 16 (Fig. 6f and l), where high resistivity and positive changes resulted in distinct peaks centered at a depth of about 45 m. An alternative approach to visualizing resistivity changes over time for such ensembles is shown in Fig. S4. Overall, these changes highlight the dynamic nature of the subsurface and suggest ongoing water movement or chemical reactions that could be affecting the subsurface resistivity distributions.

6. Discussions

This study shows a practical application of TL-ERT to monitor MAR operations using five drywells to recharge groundwater through an approximately 67 to 72 m thick vadose zone in the CCV. ERT is sensitive to changes in water content and salinity, and the array size and configuration can be adjusted to achieve the required resolution and depth of investigation. This flexibility is particularly advantageous in the CCV where the water table depth can range from a few meters to over a hundred meters deep. Furthermore, ERT can be deployed to monitor applications in areas where other tools may not be practical. For example, power lines and the highway running along the study site (Fig. 1c-d) render inductive resistivity imaging methods such as time-domain electromagnetics unusable. Still, there are complex hydrogeochemical changes occurring in the vadose zone at our study site that result in uncertainty when interpreting our TL-ERT profiles.

In this study, we proposed an ensemble approach to analyze TL-ERT data from a MAR site while minimizing model artifacts and providing uncertainty estimates. To demonstrate the applicability of our ensemble method, we compared it to a traditional approach. Our results indicated that our method produces outcomes more closely aligned with our overall understanding of the field site (e.g., based on the driller's log and point sensors data) than those obtained with the traditional approach, as outlined in Section 5.2. Therefore, when discussing the results from our MAR field site below, we will primarily reference results from our ensemble approach.

As illustrated in Figs. 5f–j and 6h–l, the injection of water caused a general decrease in resistivity as the wetting front migrated through the subsurface, as expected (e.g., Loke et al., 2022). However, we were surprised to observe increasing resistivity in certain zones of the resistivity model. As seen in Fig. 3b, the water content in early 2024 was higher compared to background levels at the start of the experiment in early 2023 for all ports, suggesting the resistivity should be lower by the end of the experiment. Instead, we propose that we are also imaging solute transport, where a decrease in pore fluid salinity will produce an increase in resistivity (e.g., García-Menéndez et al., 2018). Our results suggest that salt transport is sufficient to counteract the effect of increasing water content, which would typically decrease resistivity. For example, our point sensor at 44.5 m indicated an increase in water content from 0.17 m^3/m^3 to 0.27 m^3/m^3 when the ERT0 and ERT9 data sets were acquired (Fig. 3b). However, the model differences between ERT9 and ERT0 (Fig. 6l) indicate a significant increase in resistivity at approximately 45 m depth. This suggests that salinity must have decreased in this zone to account for the overall increase in resistivity despite the higher water content. Salt transport is consistent with the soil sensor data in Fig. 3b–c, which shows increases in both water content and electrical conductivity when the initial pulse of water reaches the sensors in mid-May. While the water content remains high, the estimated pore fluid conductivity decreases over time, indicating a change in solute concentration. Further analysis is needed to quantify the link between resistivity, water content, and salinity, for example, by using the petrophysical models proposed by Archie (1942) and Waxman & Smits (1968).

Despite the complex behavior of the resistivity changes with time (as seen in Figs. 5f–j and 6h–l), the overall trend indicates that we are observing the migration of a wetting front through the subsurface. In general, we observe decreases in resistivity where the initial resistivity was quite high, and resistivity increases where the initial resistivity was relatively low. Although these correlations are not perfect, they do suggest that the relatively fresh infiltration water displaces the in-situ pore water (presumably of higher salinity) and likely also dissolves precipitated salts in the soil pore space and transports them deeper in the vadose zone. These processes increase resistivity in areas where salt was flushed out and decrease resistivity where saline water is stored during ERT data collection.

Our analysis of the ERT results is complicated by the monitoring well data. For example, we observe a decrease in resistivity at 50 m depth as early as May 2023 (ERT2, Fig. 5g), but in the monitoring well, we do not see a substantial increase in water content in the 44.5 m port until mid-September, and no change in the estimated pore fluid conductivity. On the other hand, the water table level (Fig. 3a, right axis) shows that from time steps ERT1 and ERT2, there is a recovery of the water table of about 1 m. Several factors can contribute to this discrepancy. First, drywells were not operated continuously in parallel, partly because preliminary evaluations of the geotextile membranes at each drywell were conducted to reduce the risk of clogging, and partly due to water availability constraints. The main operations of DW1, DW2, DW3, DW4, and DW5 started on May 11, May 13, April 20, May 4, and May 14, 2023, respectively. Consequently, some non-uniformity of the wetting front is to be expected. Small-scale subsurface heterogeneity and preferential flow pathways that are not captured by ERT can also produce some bypassing of point sensors in the monitoring well (e.g., Daily et al., 1992; Park, 1998; Arora et al., 2019). Another possible explanation could be that the ERT is sensitive to the recharge water from the adjacent Flood-MAR field. Unfortunately, we were unable to run any TL-ERT cross lines that would have helped isolate the effect of the Flood-MAR field from the drywell water. However, numerical modeling of water migration from an infiltration basin into heterogeneous vadose zone systems shows that the horizontal spreading of migrating water is not expected to interfere with the drywell wetting front where the ERT measurements were taken (Sasidharan et al., 2021). Additional research is needed to fully resolve this issue.

With the ERT data acquired after the cessation of MAR operations that supplied water to both the drywells and the flood-MAR fields, we can image the long-term behavior of the vadose zone when no additional water was added to the system. While we observe some changes in the subsurface between September and November 2023, there are a few changes from November to February 2024 (see Figs. S3 and S4). We believe that without additional infiltration forcing the system, the water in the vadose zone only very slowly migrates toward the water table. Furthermore, we observe the development of a perched water table at around 25–30 m depth, where a laterally continuous low-resistivity layer forms. When using a standard time-lapse approach, such a perched layer was not imaged (see Fig. 4), although the point sensor data at a depth of 26.5 m (Fig. 3b) indicate that there are no significant changes in water content since the end of May, when it increased from 0.1 to 0.45 m^3/m^3. This supports our interpretation that a perched layer exists. Furthermore, the geological log reveals a sandy layer at 26–30 m depth overlying finer materials, which may have low vertical hydraulic conductivity, supporting a perched unit above. Such a perched water layer might not reach the groundwater table and thus will not contribute directly to recharge without the addition of more infiltration water. These results have consequences for MAR planning and execution.

To account for uncertainty estimates in our resistivity models, we inverted the TL-ERT data using a range of fixed regularization parameters (i.e., correlation lengths scales and λ, see Table 2) over time to produce an ensemble of resistivity models at each time step. Alluvial and lacustrine depositional systems such as the CCV can often be described in terms of lateral and vertical correlation length scales, although we had limited knowledge of the actual magnitude of these length scales. First, insufficient well-log coverage is available to accurately estimate the true correlation lengths at Terranova. Second, the variable lateral and vertical resolution of the ERT system meant that the recovered model length scales would not match the true length scales, even if we did know them. For these reasons, exploring a range of correlation length scales and assessing an ensemble of solutions makes sense. In the shallow subsurface where the model was well resolved, we see that the models generally converge on a relatively narrow set of solutions, as seen in the top 20 m of Fig. 6b–f. This indicates that the geostatistical constraints are given comparatively low weight compared to the data misfit term in Eq. (1). At greater depths, however, these constraints begin to matter more, as we observe an increase in the ensemble standard deviation, indicating that these are poorly resolved regions of the model.

It is crucial to emphasize that while our methodology provides a comprehensive overview of model uncertainties, it does not cover the entire spectrum of uncertainties. For example, the assumption of a homogeneous starting/reference model can significantly influence the inverted model, particularly in deep and low-sensitivity areas where the resulting resistivity values may converge towards those of the homogeneous model (e.g., Hermans et al., 2012). Additionally, parameters assumed in the covariance model (e.g., nugget effect and range) can lead to varied model representations and, consequently, different statistics of the model ensembles. In this context, geostatistically constrained inversion serves as a regularization technique that typically produces smooth results, where the correlation length scales of the inverted models may not align with the assumed geostatistical parameters (e.g., Hermans et al., 2012; Grünenbaum et al., 2023). Finally, the choice of noise models may play a critical role in the time-lapse analysis (e.g., Lesparre et al., 2017). Although we recognize the challenges of deriving realistic error estimates, we further stress the need to thoroughly explore additional error metrics, as these can significantly impact the resulting ensemble.

Future work will focus on refining our understanding of the hydrogeology of our field site in Terranova and quantifying water content changes as a function of resistivity changes. The spatially varying and competing influence of pore fluid salinity as well as the unknown impact of water from the adjacent flood-MAR field are significant obstacles for water content estimation. It is possible that the initial drywell MAR operations in 2023 have flushed most of the salts out of the vadose zone, so future infiltration will not be so heavily impacted by salinity gradients. To understand the impact of the adjacent flood-MAR field, we can conduct 3D modeling exercises to gauge the sensitivity of our ERT array to off-angle changes in resistivity. If we can isolate the effect of changing water content on our resistivity models, we can use our ensemble of models to quantify the uncertainty in this relationship at each time step. Further work can also explore the use of alternate inversion strategies that preserve the ensemble approach but impose time-lapse constraints, such as inverting for the resistivity ratios (Daily et al., 1992).

7. Conclusions

In this study, we were able to use TL-ERT to image the propagation of the wetting front from a drywell MAR experiment in California's Central Valley. We proposed an alternative to traditional time-lapse approaches where we generated ensembles of independent model solutions at each time step instead of relying on single inversion runs per time step. These ensembles were generated by implementing a geostatistical regularization and varying the correlation lengths over a predetermined range. This approach ensured that the mean models from each ensemble exhibited consistent behavior across time, appearing to reduce model artifacts typically associated with time-lapse inversions. The ERT models successfully imaged the downward propagation of the wetting front, although the migration of salts in the vadose zone complicated our interpretation considerably. Ongoing ERT data acquisition suggests that the migration of the wetting front slowed considerably after the cessation of MAR operations. Our results show that ERT can be effective for monitoring infiltration during MAR operations in complex, deep vadose zone systems. Furthermore, our ERT inversion approach holds promise for stabilizing time-lapse inversions while also providing a simple means of quantifying uncertainty in the final ERT solutions.

CRediT authorship contribution statement

Mauricio Arboleda-Zapata: Writing – review & editing, Writing – original draft, Visualization, Software, Methodology, Investigation, Formal analysis, Data curation, Conceptualization. **Gordon Osterman:** Writing – review & editing, Writing – original draft, Visualization, Validation, Supervision, Methodology, Investigation, Formal analysis, Conceptualization. **Xinyan Li:** Writing – original draft, Validation, Conceptualization. **Salini Sasidharan:** Writing – review & editing, Validation, Investigation, Data curation. **Helen E. Dahlke:** Writing – review & editing, Validation, Supervision, Resources, Project administration, Funding acquisition, Conceptualization. **Scott A. Bradford:** Writing – review & editing, Validation, Supervision, Project administration, Methodology, Investigation, Funding acquisition, Conceptualization.

Funding

This manuscript was partially funded by the United States Department of Agriculture National Program 211 and NIFA grant awards 2021-67019-33695 and 2021-68012-35914.

Declaration of competing interest

The authors declare that they have no known competing financial interests or personal relationships that could have appeared to influence the work reported in this paper.

Acknowledgments

We thank Don Cameron and his team at the Terranova Ranch for allowing us to perform this managed aquifer recharge experiment and perform ERT measurements on his property. We appreciate the support from Susan Glasser (USDA-ARS), as well as William Lennon, Andrew Silverstein, and Charlie Chen (University of California, Davis), and Raymond Hess (San Jose State University) in the fieldwork. We thank Prof. Sebastian Uhlemann and Prof. Thomas Hermans for their valuable comments and suggestions, which helped enhance this manuscript.

Appendix A. Supplementary data

Supplementary data to this article can be found online at https://doi.org/10.1016/j.jhydrol.2025.133282.

Data availability

The data and scripts for this manuscript will be publicly available after publication

References

Arboleda-Zapata, M., Guillemoteau, J., Tronicke, J., 2022. A comprehensive workflow to analyze ensembles of globally inverted 2D electrical resistivity models. *J. Appl. Geophys.* 196, 104512. https://doi.org/10.1016/j.jappgeo.2021.104512.

Arboleda-Zapata, M., Guillemoteau, J., Lucía, A., Eberle, J., Tronicke, J., Korup, O., 2023. Tracing past extreme floods on an alluvial fan using geophysical surveying. *Earth Surf. Proc. Land.* 48 (15), 3273–3286. https://doi.org/10.1002/esp.5695.

Archie, G.E., 1942. The electrical resistivity log as an aid in determining some reservoir characteristics. *Trans. AIME* 146 (01), 54–62. https://doi.org/10.2118/942054-G.

Arora, B., Dwivedi, D., Faybishenko, B., Jana, R.B., Wainwright, H.M., 2019. Understanding and Predicting Vadose Zone Processes Vol. 85, 303–328. https://doi.org/10.2138/rmg.2019.85.10.

Audebert, M., Clément, R., Touze-Foltz, N., Günther, T., Moreau, S., Duquennoi, C., 2014. Time-lapse ERT interpretation methodology for leachate injection monitoring based on multiple inversions and a clustering strategy (MICS). *J. Appl. Geophys.* 111, 320–333. https://doi.org/10.1016/j.jappgeo.2014.09.024.

Binley, A., Slater, L., 2020. *Resistivity and Induced Polarization.* Cambridge University Press https://doi.org/10.1017/9781108685955.

Blanchy, G., Saneiyan, S., Boyd, J., McLachlan, P., Binley, A., 2020. ResIPy, an intuitive open source software for complex geoelectrical inversion/modeling. *Comput. Geosci.* 137, 104423. https://doi.org/10.1016/j.cageo.2020.104423.

Bouwer, H., 2002. Artificial recharge of groundwater: hydrogeology and engineering. *Hydrgeol. J.* 10 (1), 121–142. https://doi.org/10.1007/s10040-001-0182-4.

California Department of Water Resources, . *Sustainable Groundwater Management Act*. Retrieved from https://water.ca.gov/Programs/Groundwater-Management/SGMA-Groundwater-Management (last accessed: 09/16/2024 .

California State Water Resources Control Board, 2023. Governor's Executive Orders N-7-23 & N-4-23 For Flood Diversion for Groundwater Recharge. https://www.waterboards.ca.gov/waterrights/water_issues/programs/groundwater-recharge/ (Last accessed: 09/16/2024).

Caterina, D., Hermans, T., Nguyen, F., 2014. Case studies of incorporation of prior information in electrical resistivity tomography: Comparison of different approaches. *Near Surf. Geophys.* 12 (4), 451–465. https://doi.org/10.3997/1873-0604.2013070.

Comte, J.C., Cassidy, R., Nitsche, J., Ofterdinger, U., Pilatova, K., Flynn, R., 2012. The typology of Irish hard-rock aquifers based on an integrated hydrogeological and geophysical approach. *Hydrgeol. J.* 20 (8), 1569–1588. https://doi.org/10.1007/s10040-012-0884-9.

Dahlke, H.E., LaHue, G.T., Mautner, M.R.L., Murphy, N.P., Patterson, N.K., Waterhouse, H., Yang, F., Foglia, L., 2018. Managed aquifer recharge as a tool to enhance sustainable groundwater management in California: Examples from field and modeling studies. In: *Advances in Chemical Pollution, Environmental Management and Protection*, vol. 3. Elsevier B.V, pp. 215–275. https://doi.org/10.1016/bs.apmp.2018.07.003.

Daily, W., Ramirez, A., LaBrecque, D., Nitao, J., 1992. Electrical resistivity tomography of vadose water movement. *Water Resour. Res.* 28 (5), 1429–1442. https://doi.org/10.1029/91WR03087.

de Franco, R., Biella, G., Tosi, L., Teatini, P., Lozej, A., Chiozzotto, B., Giada, M., Rizzetto, F., Claude, C., Mayer, A., Bassan, V., Gasparetto-Stori, G., 2009. Monitoring the saltwater intrusion by time lapse electrical resistivity tomography: The Chioggia test site (Venice Lagoon, Italy). *J. Appl. Geophys.* 69, 117–130. https://doi.org/10.1016/j.jappgeo.2009.08.004.

Dietrich, S., Carrera, J., Weinzettel, P., Sierra, L., 2018. Estimation of specific yield and its variability by electrical resistivity tomography. *Water Resour. Res.* 54 (11), 8653–8673. https://doi.org/10.1029/2018WR022938.

Dillon, P., Stuyfzand, P., Grischek, T., Lluria, M., Pyne, R.D.G., Jain, R.C., Bear, J., Schwarz, J., Wang, W., Fernandez, E., Stefan, C., Pettenati, M., van der Gun, J., Sprenger, C., Massmann, G., Scanlon, B.R., Xanke, J., Jokela, P., Zheng, Y., Sapiano, M., 2019. Sixty years of global progress in managed aquifer recharge. *Hydrgeol. J.* 27 (1), 1–30. https://doi.org/10.1007/s10040-018-1841-z.

Edwards, E.C., Harter, T., Fogg, G.E., Washburn, B., Hamad, H., 2016. Assessing the effectiveness of drywells as tools for stormwater management and aquifer recharge and their groundwater contamination potential. *J. Hydrol.* 539, 539–553. https://doi.org/10.1016/j.jhydrol.2016.05.059.

Faunt, C.C., Hanson, R.T., Belitz, K., 2009. Introduction, overview of hydrogeology, and textural model of California's Central Valley. In: Faunt, C.C. (Ed.), *Groundwater Availability of the Central Valley Aquifer, California.* U.S. Geological Survey, pp. 1–57.

Faunt, C.C., Belitz, K., Hanson, R.T., 2010. Development of a three-dimensional model of sedimentary texture in valley-fill deposits of Central Valley, California, USA. *Hydrgeol. J.* 18 (3), 625–649. https://doi.org/10.1007/s10040-009-0539-7.

Faunt, C.C., Sneed, M., Traum, J., Brandt, J.T., 2016. Water availability and land subsidence in the Central Valley, California, USA. *Hydrgeol. J.* 24 (3), 675–684. https://doi.org/10.1007/s10040-015-1339-x.

Furman, A., Ferre, T.P.A., Warrick, A.W., 2003. A sensitivity analysis of electrical resistivity tomography array types using analytical element modeling. *Vadose Zone Journal* 2 (3), 416–423. https://doi.org/10.2113/2.3.416.

Galloway, D.L., Burbey, T.J., 2011. Review: Regional land subsidence accompanying groundwater extraction. *Hydrgeol. J.* 19 (8), 1459–1486. https://doi.org/10.1007/s10040-011-0775-5.

García-Menéndez, O., Ballesteros, B.J., Renau-Pruñonosa, A., Morell, I., Mochales, T., Ibarra, P.I., Rubio, F.M., 2018. Using electrical resistivity tomography to assess the effectiveness of managed aquifer recharge in a salinized coastal aquifer. *Environ. Monit. Assess.* 190 (2), 100. https://doi.org/10.1007/s10661-017-6446-9.

Gelhar, L.W., 1993. *Stochastic subsurface hydrology*. Prentice-Hall Inc.

Grünenbaum, N., Günther, T., Greskowiak, J., Vienken, T., Müller-Petke, M., Massmann, G., 2023. Salinity distribution in the subterranean estuary of a meso-tidal high-energy beach characterized by Electrical Resistivity Tomography and direct push technology. *J. Hydrol. 617*, 129074. https://doi.org/10.1016/j.jhydrol.2023.129074.

Günther, T., Rücker, C., Spitzer, K., 2006. Three-dimensional modelling and inversion of dc resistivity data incorporating topography - II. Inversion. *Geophysical Journal International*, *166*(2), 506–517. https://doi.org/10.1111/j.1365-246X.2006.03011.x.

Gvirtzman, H., Shalev, E., Dahan, O., Hatzor, Y.H., 2008. Large-scale infiltration experiments into unsaturated stratified loess sediments: Monitoring and modeling. *J. Hydrol.* 349, 214–229. https://doi.org/10.1016/j.jhydrol.2007.11.002.

Haaken, K., Furman, A., Weisbrod, N., Kemna, A., 2016. Time-lapse electrical imaging of water infiltration in the context of soil aquifer treatment. *Vadose Zone J.* 15 (11), 1–12. https://doi.org/10.2136/vzj2016.04.0028.

Hayley, K., Bentley, L.R., Pidlisecky, A., 2010. Compensating for temperature variations in time-lapse electrical resistivity difference imaging. Geophysics 75 (4), WA51–WA59. https://doi.org/10.1190/1.3478208.

Hermans, T., Vandenbohede, A., Lebbe, L., Martin, R., Kemna, A., Beaujean, J., Nguyen, F., 2012a. Imaging artificial salt water infiltration using electrical resistivity tomography constrained by geostatistical data. *J. Hydrol.* 438–439, 168–180. https://doi.org/10.1016/j.jhydrol.2012.03.021.

Hermans, T., Irving, J., 2017. Facies discrimination with electrical resistivity tomography using a probabilistic methodology: effect of sensitivity and regularisation. *Near Surf. Geophys.* 15 (1), 13–25. https://doi.org/10.3997/1873-0604.2016047.

Hermans, T., Vandenbohede, A., Lebbe, L., Martin, R., Kemna, A., Beaujean, J., Nguyen, F., 2012b. Imaging artificial salt water infiltration using electrical resistivity tomography constrained by geostatistical data. *J. Hydrol.* 438–439, 168–180. https://doi.org/10.1016/j.jhydrol.2012.03.021.

Hermans, T., Vandenbohede, A., Lebbe, L., Martin, R., Kemna, A., Beaujean, J., Nguyen, F., 2012c. Imaging artificial salt water infiltration using electrical resistivity tomography constrained by geostatistical data. *J. Hydrol.* 438–439, 168–180. https://doi.org/10.1016/j.jhydrol.2012.03.021.

Hermans, T., Nguyen, F., Robert, T., Revil, A., 2014. Geophysical methods for monitoring temperature changes in shallow low enthalpy geothermal systems. *Energies* 7 (8), 5083–5118. https://doi.org/10.3390/en7085083.

Hilhorst, M. A., 2000. A Pore water conductivity sensor. Soil Sci. Soc. Am. J. 64(6), 1922-1925. https://doi.org/10.2136/sssaj2000.6461922x.

Jasechko, S., Perrone, D., 2020. California's Central Valley groundwater wells run dry during recent drought. *Earth's Future* 8 (4). https://doi.org/10.1029/2019EF001339.

Jeanne, P., Farr, T.G., Rutqvist, J., Vasco, D.W., 2019. Role of agricultural activity on land subsidence in the San Joaquin Valley, California. *J. Hydrol.* 569, 462–469. https://doi.org/10.1016/j.jhydrol.2018.11.077.

Johnson, T., Versteeg, R., Thomle, J., Hammond, G., Chen, X., Zachara, J., 2015. Four-dimensional electrical conductivity monitoring of stage-driven river water intrusion: Accounting for water table effects using a transient mesh boundary and conditional inversion constraints. *Water Resour. Res.* 51 (8), 6177–6196. https://doi.org/10.1002/2014WR016129.

Jordi, C., Doetsch, J., Günther, T., Schmelzbach, C., Robertsson, J.O.A., 2018. Geostatistical regularization operators for geophysical inverse problems on irregular meshes. *Geophys. J. Int.* 213 (2), 1374–1386. https://doi.org/10.1093/GJI/GGY055.

Kang, S., Knight, R., 2023. Isolating the poroelastic response of the groundwater system in InSAR data from the Central Valley of California. *Geophys. Res. Lett.* 50 (9), e2023GL103222. https://doi.org/10.1029/2023GL103222.

Kang, S., Knight, R., Greene, T., Buck, C., Fogg, G., 2021. Exploring the model space of airborne electromagnetic data to delineate large-scale structure and heterogeneity within an aquifer system. *Water Resour. Res.* 57 (10), e2021WR029699. https://doi.org/10.1029/2021WR029699.

Kim, J.H., Supper, R., Tsourlos, P., Yi, M.J., 2013. Four-dimensional inversion of resistivity monitoring data through Lp norm minimizations. *Geophys. J. Int.* 195 (3), 1640–1656. https://doi.org/10.1093/gji/ggt324.

Kocis, T.N., Dahlke, H.E., 2017. Availability of high-magnitude streamflow for groundwater banking in the Central Valley, California. *Environ. Res. Lett.* 12 (8), 084009. https://doi.org/10.1088/1748-9326/aa7b1b.

Koestel, J., Kemna, A., Javaux, M., Binley, A., Vereecken, H., 2008. Quantitative imaging of solute transport in an unsaturated and undisturbed soil monolith with 3-D ERT and TDR. *Water Resour. Res.* 44 (12), W12411. https://doi.org/10.1029/2007WR006755.

LaBrecque, D.J., Yang, X., 2001. Difference inversion of ERT data: a fast inversion method for 3-D in situ monitoring. *J. Environ. Eng. Geophys.* 6 (2), 83–89. https://doi.org/10.4133/jeeg6.2.83.

Labrecque, D.J., Miletto, M., Daily, W., Ramirez, A., Owen, E., 1996. The effects of noise on Occam's inversion of resistivity tomography data. *Geophysics* 61 (2), 538–548. https://doi.org/10.1190/1.1443980.

Lesparre, N., Nguyen, F., Kemna, A., Robert, T., Hermans, T., Daoudi, M., & Flores-Orozco, A. (2017). A new approach for time-lapse data weighting in electrical resistivity tomography. *Geophysics*, *82*(6), E325–E333. https://doi.org/10.1190/GEO2017-0024.1.

Levintal, E., Kniffin, M.L., Ganot, Y., Marwaha, N., Murphy, N.P., Dahlke, H.E., 2023. Agricultural managed aquifer recharge (Ag-MAR)—a method for sustainable groundwater management: A review. *Crit. Rev. Environ. Sci. Technol.* 53 (3), 291–314. https://doi.org/10.1080/10643389.2022.2050160.

Liu, R., Zhao, Y., Cao, G., Wang, Q., Ma, M., Li, E., Deng, H., 2022. Threat of land subsidence to the groundwater supply capacity of a multi-layer aquifer system. *J. Hydrol.: Reg. Stud. 44*, 101240. https://doi.org/10.1016/j.ejrh.2022.101240.

Loke, M.H., Wilkinson, P.B., Chambers, J.E., Uhlemann, S., Dijkstra, T., Dahlin, T., 2022. The use of asymmetric time constraints in 4-D ERT inversion. *J. Appl. Geophys.* 197. https://doi.org/10.1016/j.jappgeo.2022.104536.

Michot, D., Benderitter, Y., Dorigny, A., Nicoullaud, B., King, D., Tabbagh, A., 2003. Spatial and temporal monitoring of soil water content with an irrigated corn crop cover using surface electrical resistivity tomography. *Water Resour. Res.* 39 (5), 1138. https://doi.org/10.1029/2002WR001581.

Miller, C.R., Routh, P.S., Brosten, T.R., McNamara, J.P., 2008. Application of time-lapse ERT imaging to watershed characterization. *Geophysics* 73 (3), G7–G17. https://doi.org/10.1190/1.2907156.

Müller, S., Schüler, L., Zech, A., Heße, F., 2022. GSTools v1.3: A toolbox for geostatistical modelling in Python. Geosci. Model Dev. 15 (7), 3161–3182. https://doi.org/10.5194/gmd-15-3161-2022.

Müller, K., Vanderborght, J., Englert, A., Kemna, A., Huisman, J.A., Rings, J., Vereecken, H., 2010. Imaging and characterization of solute transport during two tracer tests in a shallow aquifer using electrical resistivity tomography and multilevel groundwater samplers. *Water Resour. Res.* 46 (3). https://doi.org/10.1029/2008WR007595.

Musgrave, H., Binley, A., 2011. Revealing the temporal dynamics of subsurface temperature in a wetland using time-lapse geophysics. *J. Hydrol.* 396 (3–4), 258–266. https://doi.org/10.1016/j.jhydrol.2010.11.008.

Ogunmokun, F.A., Wallach, R., 2021. Remediating the adverse effects of treated wastewater irrigation by repeated on-surface surfactant application. *Water Resour. Res.* 57 (6), e2020WR029429. https://doi.org/10.1029/2020WR029429.

Oldenborger, G. A., Knoll, M. D., Routh, P. S., LaBrecque, D. J., 2007. Time-lapse ERT monitoring of an injection/withdrawal experiment in a shallow unconfined aquifer. *Geophysics*, *72*(4), F177–F187. https://doi.org/10.1190/1.2734365.

Palacios, A., José Ledo, J., Linde, N., Luquot, L., Bellmunt, F., Folch, A., Marcuello, A., Queralt, P., A. Pezard, P., Martínez, L., del Val, L., Bosch, D., Carrera, J., 2020. Time-lapse cross-hole electrical resistivity tomography (CHERT) for monitoring seawater intrusion dynamics in a Mediterranean aquifer. *Hydrol. Earth Syst. Sci. 24*(4), 2121–2139. https://doi.org/10.5194/hess-24-2121-2020.

Park, S., 1998. Fluid migration in the vadose zone from 3-D inversion of resistivity monitoring data. *Geophysics* 63 (1), 41–51. https://doi.org/10.1190/1.1444326.

Pereira, J.L., Gómez-Hernández, J.J., Zanini, A., Varouchakis, E.A., Azevedo, L., 2023. Iterative geostatistical electrical resistivity tomography inversion. *Hydrgeol. J.* 31 (6), 1627–1645. https://doi.org/10.1007/s10040-023-02683-w.

Perrone, A., Lapenna, V., Piscitelli, S., 2014. Electrical resistivity tomography technique for landslide investigation: A review. *Earth Sci. Rev.* 135, 65–82. https://doi.org/10.1016/j.earscirev.2014.04.002.

Perzan, Z., Osterman, G., Maher, K., 2023. Controls on flood managed aquifer recharge through a heterogeneous vadose zone: hydrologic modeling at a site characterized with surface geophysics. *Hydrol. Earth Syst. Sci.* 27 (5), 969–990. https://doi.org/10.5194/hess-27-969-2023.

Pleasants, M.S., Neves, F. dos A., Parsekian, A.D., Befus, K.M., Kelleners, T.J., 2022. Hydrogeophysical inversion of time-lapse ERT data to determine hillslope subsurface hydraulic properties. *Water Resour. Res.* 58 (4), e2021WR031073. https://doi.org/10.1029/2021WR031073.

Ramirez, A.L., Nitao, J.J., Hanley, W.G., Aines, R., Glaser, R.E., Sengupta, S.K., Daily, W. D., 2005. Stochastic inversion of electrical resistivity changes using a Markov Chain Monte Carlo approach. *J. Geophys. Res. Solid Earth* 110 (2), B02101. https://doi.org/10.1029/2004JB003449.

Ringleb, J., Sallwey, J., Stefan, C., 2016. Assessment of managed aquifer recharge through modeling—a review. *Water* 8 (12), 579. https://doi.org/10.3390/w8120579.

Rücker, C., Günther, T., Spitzer, K., 2006. Three-dimensional modelling and inversion of dc resistivity data incorporating topography – I. Modelling. *Geophys. J. Int.* 166 (2), 495–505. https://doi.org/10.1111/j.1365-246X.2006.03010.x.

Rücker, C., Günther, T., Wagner, F.M., 2017. 12). pyGIMLi: An open-source library for modelling and inversion in geophysics. *Comput. Geosci.* 109, 106–123. https://doi.org/10.1016/j.cageo.2017.07.011.

Sasidharan, S., Bradford, S.A., Šimůnek, J., DeJong, B., Kraemer, S.R., 2018. Evaluating drywells for stormwater management and enhanced aquifer recharge. *Adv. Water Resour.* 116, 167–177. https://doi.org/10.1016/j.advwatres.2018.04.003.

Sasidharan, S., Bradford, S.A., Šimůnek, J., Kraemer, S.R., 2020. Groundwater recharge from drywells under constant head conditions. *J. Hydrol.* 583, 124569. https://doi.org/10.1016/j.jhydrol.2020.124569.

Sasidharan, S., Bradford, S.A., Šimůnek, J., Kraemer, S.R., 2021. Comparison of recharge from drywells and infiltration basins: A modeling study. *J. Hydrol.* 594, 125720. https://doi.org/10.1016/j.jhydrol.2020.125720.
Sendrós, A., Himi, M., Lovera, R., Rivero, L., Garcia-Artigas, R., Urruela, A., Casas, A., 2020. Electrical resistivity tomography monitoring of two managed aquifer recharge ponds in the alluvial aquifer of the Llobregat River (Barcelona, Spain). *Near Surf. Geophys.* 18 (4), 353–368. https://doi.org/10.1002/nsg.12113.
Singha, K., Day-Lewis, F.D., Johnson, T., Slater, L.D., 2015. Advances in interpretation of subsurface processes with time-lapse electrical imaging. *Hydrol. Process.* 29, 1549–1576. https://doi.org/10.1002/HYP.10280.
Slater, L., Binley, A.M., Daily, W., Johnson, R., 2000. Cross-hole electrical imaging of a controlled saline tracer injection. *J. Appl. Geophys.* 44 (2–3), 85–102. https://doi.org/10.1016/S0926-9851(00)00002-1.
Stummer, P., Maurer, H., Green, A.G., 2004. Experimental design: Electrical resistivity data sets that provide optimum subsurface information. *Geophysics* 69 (1), 120–139. https://doi.org/10.1190/1.1649381.
Tronicke, J., Holliger, K., 2005. Quantitative integration of hydrogeophysical data: Conditional geostatistical simulation for characterizing heterogeneous alluvial aquifers. *Geophysics* 70 (3), H1–H10. https://doi.org/10.1190/1.1925744.
Tso, C.-H.-M., Kuras, O., Wilkinson, P.B., Uhlemann, S., Chambers, J.E., Meldrum, P.I., Graham, J., Sherlock, E.F., Binley, A., 2017. Improved characterisation and modelling of measurement errors in electrical resistivity tomography (ERT) surveys. *J. Appl. Geophys.* 146, 103–119. https://doi.org/10.1016/j.jappgeo.2017.09.009.
Uhlemann, S., Peruzzo, L., Chou, C., Williams, K.H., Wielandt, S., Wang, C., Falco, N., Wu, Y., Carr, B., Meldrum, P., Chambers, J., Dafflon, B., 2024. Variations in bedrock and vegetation cover modulate subsurface water flow dynamics of a mountainous hillslope. *Water Resour. Res.* 60 (2), e2023WR036137. https://doi.org/10.1029/2023WR036137.
Uhlemann, S.S., Sorensen, J.P., House, A.R., Wilkinson, P.B., Roberts, C., Gooddy, D.C., Chambers, J.E., 2016. Integrated time-lapse geoelectrical imaging of wetland hydrological processes. *Water Resour. Res.* 52 (3), 1607–1625. https://doi.org/10.1002/2015WR017932.
Uhlemann, S., Ulrich, C., Newcomer, M., Fiske, P., Kim, J., Pope, J., 2022. 3D hydrogeophysical characterization of managed aquifer recharge basins. *Front. Earth Sci.* 10, 1–13. https://doi.org/10.3389/feart.2022.942737.
Waxman, M.H., Smits, L.J.M., 1968. Electrical conductivities in oil-bearing shaly sands. *Soc. Pet. Eng. J.* 8 (02), 107–122. https://doi.org/10.2118/1863-A.
Whiteley, J.S., Chambers, J.E., Uhlemann, S., Wilkinson, P.B., Kendall, J.M., 2019. Geophysical monitoring of moisture-induced landslides: a review. *Rev. Geophys.* 57 (1), 106–145. https://doi.org/10.1029/2018RG000603.
Wilkinson, P.B., Chambers, J.E., Meldrum, P.I., Kuras, O., Inauen, C.M., Swift, R.T., Curioni, G., Uhlemann, S., Graham, J., Atherton, N., 2022. Windowed 4D inversion for near real-time geoelectrical monitoring applications. *Front. Earth Sci.* 10. https://doi.org/10.3389/feart.2022.983603.
Yeh, T.-C.-J., Liu, S., Glass, R.J., Baker, K., Brainard, J.R., Alumbaugh, D., LaBrecque, D., 2002. A geostatistically based inverse model for electrical resistivity surveys and its applications to vadose zone hydrology. *Water Resour. Res.* 38 (12), 1278. https://doi.org/10.1029/2001WR001204.
Zhou, B., Dahlin, T., 2003. Properties and effects of measurement errors on 2D resistivity imaging surveying. *Near Surf. Geophys.* 1 (3), 105–117. https://doi.org/10.3997/1873-0604.2003001.
Zhou, T., Ruud, N., Šimůnek, J., Brunetti, G., Levintal, E., García, C.P., Dahlke, H.E., 2024. The impact of managed aquifer recharge on the fate and transport of pesticides in agricultural soils. *Water Res.* 267, 122442. https://doi.org/10.1016/j.watres.2024.122442.